

Lawrence Berkeley National Laboratory

LBL Publications

Title

Direct observation of minibands in a twisted graphene/WS₂ bilayer

Permalink

<https://escholarship.org/uc/item/1vg1p93c>

Journal

Science Advances, 6(14)

ISSN

2375-2548

Authors

Ulstrup, Søren

Koch, Roland J

Singh, Simranjeet

et al.

Publication Date

2020-04-03

DOI

10.1126/sciadv.aay6104

Peer reviewed

MATERIALS SCIENCE

Direct observation of minibands in a twisted graphene/WS₂ bilayer

Søren Ulstrup^{1*†}, Roland J. Koch^{2*}, Simranjeet Singh³, Kathleen M. McCreary⁴, Berend T. Jonker⁴, Jeremy T. Robinson⁴, Chris Jozwiak², Eli Rotenberg², Aaron Bostwick², Jyoti Katoch^{3†}, Jill A. Miwa^{5†}

Stacking two-dimensional (2D) van der Waals materials with different interlayer atomic registry in a heterobilayer causes the formation of a long-range periodic superlattice that may bestow the heterostructure with properties such as new quantum fractal states or superconductivity. Recent optical measurements of transition metal dichalcogenide (TMD) heterobilayers have revealed the presence of hybridized interlayer electron-hole pair excitations at energies defined by the superlattice potential. The corresponding quasiparticle band structures, so-called minibands, have remained elusive, and no such features have been reported for heterobilayers composed of a TMD and another type of 2D material. We introduce a new x-ray capillary technology for performing microfocused angle-resolved photoemission spectroscopy with a spatial resolution of $\sim 1 \mu\text{m}$, and directly observe minibands at certain twist angles in mini Brillouin zones (mBZs). We discuss their origin in terms of initial and final state effects by analyzing their dispersion in distinct mBZs.

INTRODUCTION

Assembling single-layer (SL) transition metal dichalcogenides (TMDs) with different electronic structures in heterobilayers has emerged as a promising method for tailoring the band alignment at type II heterojunctions (1, 2), offering a means to control optical excitation and charge transfer processes at the atomic scale (3). This approach to materials design inevitably involves joining two crystal lattices with different lattice constants and orientations. The long-range periodic pattern arising from the superposition of interlayer atomic registries produces a moiré superlattice. Scanning tunneling microscopy/spectroscopy (STM/STS) experiments on heterobilayers of TMDs have resolved such a moiré together with a local bandgap modulation due to the superlattice potential (4). Properties defined by the superlattice potential such as new quantum fractal states (5–7) and superconductivity (8, 9) have been probed via transport measurements when these heterostructures are implemented in a device architecture. In angle-resolved photoemission spectroscopy (ARPES), these superlattice effects are directly observable via the formation of minibands such as the mini Dirac cones identified in epitaxial graphene on Ir(111) (10, 11), twisted bilayer graphene (12), and heterostructures of graphene with hexagonal boron nitride (hBN) (13, 14). Since ARPES directly probes the energy- and momentum-resolved quasiparticle excitation spectrum, these measurements provide critical information about the minibands such as dispersion, hybridization with main bands, opening of mini gaps, and emergence of correlation effects, i.e., properties that completely specify the functionality of the heterostructure.

It has so far not been possible to observe similar minibands in epitaxial SL TMDs on single-crystal metal substrates (15) or TMDs

on bilayer graphene on silicon carbide (16, 17) despite visible moiré superlattices in the STM data (15, 17, 18). Recent optical studies of TMD heterobilayers, however, show distinct exciton lines arising from twist angle-dependent minibands (19–25). It is plausible that the signature of the quasiparticle minibands may have been suppressed in these earlier ARPES measurements due to stronger TMD-substrate interactions, long-range rotational disorder, and/or quenching of the interlayer photoemission intensity as a result of the three-atomic-layer (sandwich-like) structure, which essentially constitutes a SL TMD, effectively “burying” the interface. Furthermore, the epitaxial approach in these studies did not allow for tuning of layer orientation, thereby preventing a systematic search for minibands in materials with a different moiré superlattice.

RESULTS AND DISCUSSION

We resolve these issues by using a new microfocused ARPES (microARPES) approach with a spatial resolution on the order of $1 \mu\text{m}$ to measure a heterobilayer consisting of graphene, SL WS₂, and hBN. Both the graphene and the SL WS₂ were grown by chemical vapor deposition (CVD) and sequentially transferred onto the hBN. The graphene has multiple domain orientations, while the SL WS₂ is a single domain. The resulting graphene/WS₂/hBN stack is supported on a TiO₂ wafer; see illustration in Fig. 1A and optical microscope image of hBN flakes on TiO₂ in Fig. 1B. The atomically flat interface and vanishing interlayer interactions with hBN facilitate the collection of extremely high-quality ARPES spectra as recently demonstrated for bare WS₂/hBN (26). The CVD-grown graphene provides a multitude of different orientations on top of WS₂, giving access to domains with different twist angles (θ -domains). The interface of the heterobilayer is notably situated below a single carbon layer instead of the sandwich-like structure of the SL TMD, thereby greatly enhancing the photoemission intensity from the interface compared to earlier studies. Each interface type and θ -domain are measured by scanning the microfocused beam of photons across the same area of the sample as seen in the optical microscope image in Fig. 1B, leading to photoemission from microscopic points on the

Copyright © 2020 The Authors, some rights reserved; exclusive licensee American Association for the Advancement of Science. No claim to original U.S. Government Works. Distributed under a Creative Commons Attribution NonCommercial License 4.0 (CC BY-NC).

¹Department of Physics and Astronomy, Aarhus University, 8000 Aarhus C, Denmark.

²Advanced Light Source, E. O. Lawrence Berkeley National Laboratory, Berkeley, CA 94720, USA.

³Department of Physics, Carnegie Mellon University, Pittsburgh, PA 15213, USA.

⁴Naval Research Laboratory, Washington, DC 20375, USA.

⁵Department of Physics and Astronomy, Aarhus University, 8000 Aarhus C, Denmark.

*These authors contributed equally to this work.

†Corresponding author. Email: ulstrup@phys.au.dk (S.U.); jkatoch@andrew.cmu.edu (J.K.); miwa@phys.au.dk (J.A.M.)

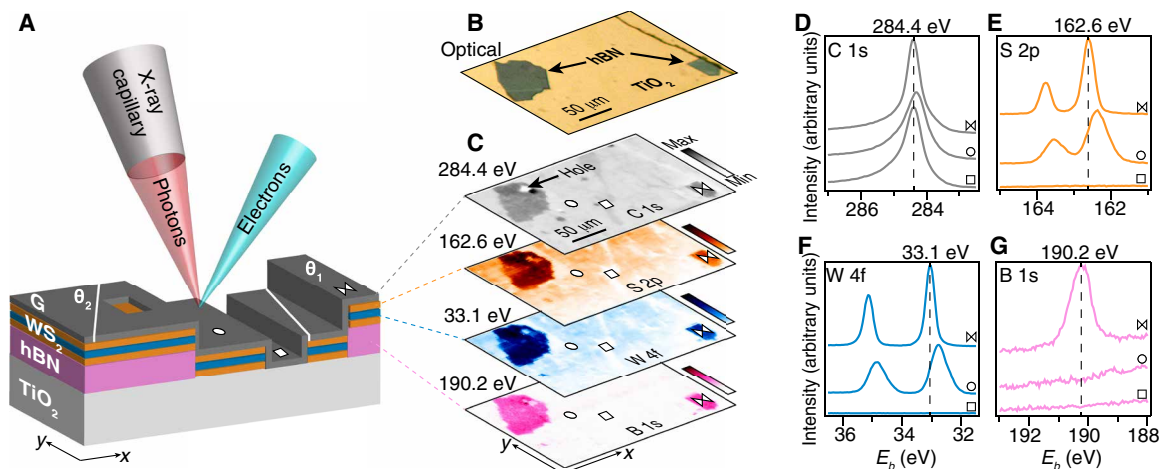


Fig. 1. Elemental mapping of heterobilayer interfaces. (A) Model of sample and photoemission setup with a microfocused beam achieved using an x-ray capillary. Differently rotated graphene domains are separated by white lines and annotated with twist angles θ_1 and θ_2 . (B) Optical microscope image of the sample. Two hBN flakes are shown via arrows. (C) Stack of (x, y) -photoemission intensity maps corresponding to the given binding energies and core level peaks collected at a photon energy of 350 eV. The hBN flakes are also visible in these maps. The arrow on the C 1s map points to a hole in the graphene flake. (D to G) Core level peaks obtained from the spots on the map in (C) labeled by corresponding symbols. The vertical dashed lines mark the binding energies used for composing the maps in (C).

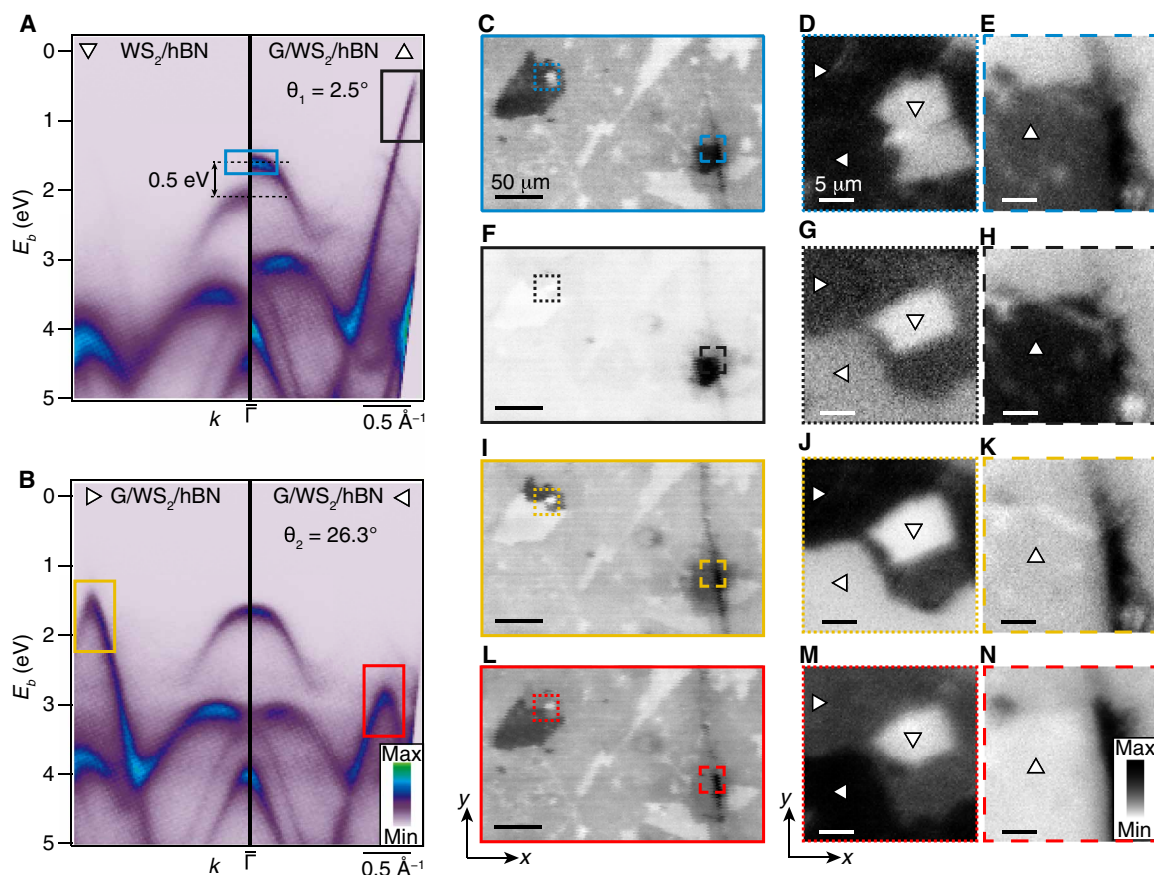


Fig. 2. Band structure mapping in real space and momentum space. (A and B) microARPES dispersion from θ -domains with the stated angles and from a bare WS₂/hBN area. The double-headed arrow and dashed lines in (A) indicate a binding energy shift of 0.5 eV of the WS₂ electronic structure on hBN in the absence of graphene. (C to N) Maps of the (x, y) -dependent photoemission intensity composed from the (E, k) -regions marked by boxes in (A) and (B) with the color coding between boxes and panels given by (C to E) blue, (F to H) black, (I to K) yellow, and (L to N) red. The fine scan maps in dotted and dashed panels are closeups of the regions demarcated by dotted and dashed boxes in the coarse scan maps in (C), (F), (I), and (L). The symbols in the fine scan maps mark the spots where the correspondingly labeled $E(k)$ dispersion cuts in (A) and (B) were obtained. The data were obtained at a photon energy of 145 eV.

sample. The focusing is achieved using an achromatic x-ray capillary, providing efficient mapping of valence band (VB) and core level binding energy regions due to a high photon flux and highly tunable photon energy range compared to conventional x-ray focusing optics such as Fresnel zone plates (27–29).

Photoemission intensity maps acquired at core level peak energies characteristic of the 2D materials in the heterostructure are shown in Fig. 1C. Each (x, y) -position in a map contains a measurement of the corresponding core level binding energy region as shown for the points marked by the symbols “□,” “⋈,” and “○” for C 1s in Fig. 1D, S 2p in Fig. 1E, W 4f in Fig. 1F, and B 1s in Fig. 1G. The contrasts provided by the peak amplitude, position, and linewidth clearly outline the graphene/TiO₂ (□), graphene/WS₂/TiO₂ (○), and graphene/WS₂/hBN/TiO₂ (⋈) interfaces. We also identify a hole in the transferred graphene, exposing a bare WS₂/hBN area as seen via an arrow in the C 1s map in Fig. 1C. The spectral linewidths of W 4f, S 2p, and C 1s core levels obtained on hBN (marked by the ⋈) are reduced by a factor of 2 compared to those measured on the TiO₂ (marked by the ○). Similar conclusions can be made for the linewidths of the VB spectra as discussed in further detail in section S1, which we attribute to the flatness and extremely weak charge impurity scattering in hBN compared to the oxide.

We determine the energy- and momentum-dependent dispersion relation, $E(k)$, in the VB region, as shown in Fig. 2 (A and B). The spectra are characterized by a mix of graphene bands (see black, yellow, and red boxes) and the WS₂ VB manifold [see blue box for the local VB maximum (VBM) at $\bar{\Gamma}$]. We find that the graphene pins the WS₂ electronic structure by a rigid shift of 0.5 eV compared with the WS₂ states measured on a bare WS₂/hBN region of the sample; see double-headed arrow in Fig. 2A. The presented data are only a subset of spectra from a four-dimensional (4D) dataset containing the (E, k, x, y) -dependent photoemission intensity. It is furthermore possible to obtain corresponding cuts of the intensity in real space composed from a specified region of (E, k) -space. The results of projecting the specified electronic band structure on a (x, y) -dependent intensity map are shown in Fig. 2 (C to N). The (x, y) -maps in Fig. 2 (C to E) are derived from the WS₂ local VBM at $\bar{\Gamma}$. The map in Fig. 2C is a coarse scan corresponding to the field of view in Fig. 1 (B and C), while the maps in Fig. 2 (D and E) are fine scans of the regions demarcated by dotted and dashed boxes in Fig. 2C. High (low) intensity in real space allows us to identify the presence (absence) of WS₂ electronic states at energies and momenta determined by the blue box in Fig. 2A. Similarly, the (x, y) -maps in Fig. 2 (F to N) track the domains with the graphene bands given by the (E, k) -cuts in the black, yellow, and red boxes in Fig. 2 (A and B). Measurements of the full 2D Brillouin zone (BZ) permit the determination of θ , as explained in section S2. Here, we focus on the two θ -domains seen via high intensity in Fig. 2 (F and L) (see also symbols “ Δ ” and “ \triangleleft ” in Fig. 2) where we find two significantly different twist angles given by $\theta_1 = (2.5 \pm 0.2)^\circ$ and $\theta_2 = (26.3 \pm 0.2)^\circ$. We also observe another orientation in Fig. 2I (marked by a “ \triangleright ” in Fig. 2), but this graphene/WS₂ interface has a 5- μm hole (marked by a “ ∇ ” in Fig. 2), which led to spurious features in the BZ maps we collected from this domain preventing a detailed analysis of the twist angle.

Maps in Fig. 3 (A and B) are in two momentum directions, k_x and k_y , the constant energy contours at a binding energy of approximately 1.6 eV for the θ_1 - and θ_2 -domains. In both maps, the three most prominent features are labeled $\bar{\Gamma}$, \bar{K}_W , and \bar{K}_G ; these labels correspond

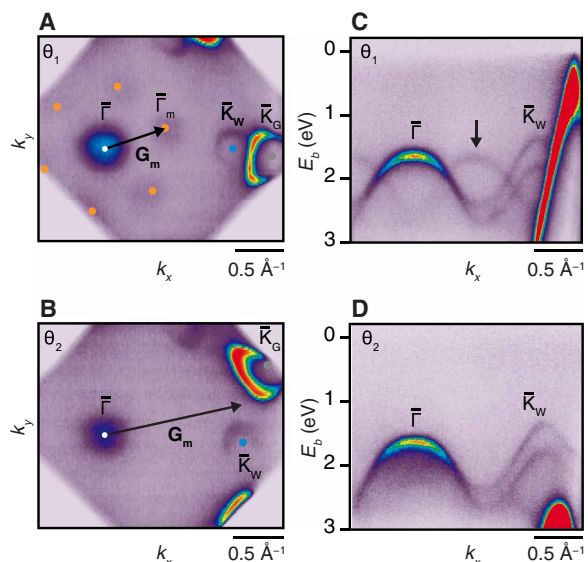


Fig. 3. Direct observation of minibands. (A) 2D BZ map acquired on the θ_1 -domain at a photon energy of 70 eV. The twist angle between the overlaying graphene and the underlying WS₂ is determined to be 2.5° , as measured from the angle between the $\bar{\Gamma}$ - \bar{K}_G and $\bar{\Gamma}$ - \bar{K}_W directions. This twist gives rise to minibands of $\bar{\Gamma}$, marked with an orange dot and labeled as $\bar{\Gamma}_m$. (B) Similar 2D BZ map acquired on the θ_2 -domain. Here, the twist angle is 26.3° . (C) The dispersion for the θ_1 -domain along the $\bar{\Gamma}$ - \bar{K}_W direction is shown with the miniband highlighted by the black arrow. (D) Similar dispersion for the θ_2 -domain where the minibands are notably absent compared with the θ_1 -domain.

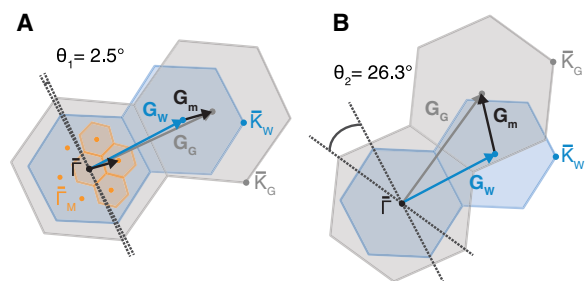


Fig. 4. Construction of BZs and WS₂ mBZs. (A) Illustration of θ_1 -domain with salient reciprocal lattice vectors denoted along with the formed mBZ. Two adjacent 2D BZs of graphene (gray) and WS₂ (blue) are overlaid with a twist angle of 2.5° . The reciprocal lattice vectors are shown for graphene (\mathbf{G}_G) and for WS₂ (\mathbf{G}_W) that give rise to the moiré reciprocal lattice vector \mathbf{G}_m (black arrow). The mBZs are constructed by replicating \mathbf{G}_m around the $\bar{\Gamma}$ point (orange). (B) Illustration similar to the one in (A) but for the θ_2 -domain.

to the nearly circular feature of the WS₂ band at $\bar{\Gamma}$, the spin-split bands of WS₂ at \bar{K}_W , and the horseshoe-shaped arcs of the graphene Dirac cones at \bar{K}_G . There are faint circular features surrounding $\bar{\Gamma}$ in Fig. 3A that are notably absent in Fig. 3B. These features are ascribed to minibands, labeled as $\bar{\Gamma}_m$. From the dispersion of the bands, acquired along the $\bar{\Gamma}$ - \bar{K}_W direction as shown in Fig. 3C, we see that the miniband, highlighted by the black arrow, replicates the overall shape of the SL WS₂ band at $\bar{\Gamma}$. No miniband is present in the similarly acquired (E, k) -plot of Fig. 3D for the θ_2 -domain where the twist between the graphene and SL WS₂ lattices is at a substantially larger angle of 26.3° . We observe that the intensity of the WS₂ minibands is maximal in a 60- to 70-eV photon energy range and that

the E - and k -dependence of the intensity does not simply follow that of the main band, as shown in section S3. This behavior can be described as an interference effect between photoemitted electrons emerging from the heterobilayer, which strongly depends on the electron kinetic energy, the interaction between layers, the origin of the emitters, and their orbital character (30). It is possible that the geometry of the heterobilayer, given by the θ_2 -domain, diminishes such an interference effect, thereby leading to an overall suppression of the minibands.

The positions of the minibands in k -space are determined by addition of the reciprocal lattice vectors of graphene (\mathbf{G}_G) and WS_2 (\mathbf{G}_W), as illustrated in Fig. 4. Two adjacent 2D BZs of graphene (gray hexagons) are superimposed on two adjacent 2D BZs of WS_2 (blue hexagons) with twist angles matching those of θ_1 - and θ_2 -domains. From the reciprocal lattice vectors, we establish the moiré reciprocal lattice vector (\mathbf{G}_m) and construct the corresponding mBZs (orange hexagons) by replicating \mathbf{G}_m around the Γ point to locate the centers (orange dots) of the surrounding mBZs. The position of the minibands is mathematically confirmed using the following expressions for the angles and magnitude of the moiré vector: $\phi_{m, G(W)} = \arctan(\sin \theta / (\cos \theta - |\mathbf{G}_{G(W)}|/|\mathbf{G}_{W(G)}|))$ and $|\mathbf{G}_m| = (G_{G(W)}^2 - |\mathbf{G}_{G(W)}||\mathbf{G}_{W(G)}| \cos \theta) / (|\mathbf{G}_{G(W)}| \cos \phi_{m, G(W)})$. We find that $|\mathbf{G}_m| = 0.66 \text{ \AA}^{-1}$ (1.35 \AA^{-1}) for the θ_1 -domain (θ_2 -domain), $\phi_{m, G} = 8.9^\circ$ (49.1°) for the angle between \mathbf{G}_m and \mathbf{G}_G , and $\phi_{m, W} = 11.4^\circ$ (75.4°) for the angle between \mathbf{G}_m and \mathbf{G}_W . All magnitudes of the reciprocal lattice vectors and angles are in agreement with the microARPES data obtained for these two domains shown in Fig. 3 within the experimental accuracy. The observation of WS_2 minibands also implies the existence of mini Dirac cones replicated by the same reciprocal lattice vector in the graphene. We find mini Dirac cones at the expected k -space coordinates, but their intensity is extremely faint, as shown in section S4. This strong suppression of intensity compared to the WS_2 minibands is likely caused by the different orbital character of the graphene π -states, leading to a substantially different E - and k -dependence of the one-electron dipole matrix elements that shape the ARPES intensity (30). The observation of Dirac cone replicas also confirms that the minibands derive from the graphene/ WS_2 and not the WS_2/hBN interface. Moreover, we do not observe any replicas from the bare WS_2/hBN interface in the hole (see the “V” in Fig. 2) nor in a previous study (26), possibly due to this interface being buried below the TMD sandwich-like structure. For the sake of clarity, we have omitted the hBN 2D BZ in the sketches in Fig. 2, as this interface does not contribute to our observations.

There are two possible explanations for the origin of the minibands. First, they may emerge due to photoelectron diffraction, which would lead to noninteracting replicas with the same intensity distribution as the main band, as observed in graphene on silicon carbide (31). In this case, one refers to the minibands as a final state effect. Second, the minibands may be caused by the periodic superlattice potential formed by the twisted WS_2 and graphene layers. A direct evidence of such an initial state effect would be the opening of mini gaps at the mBZ boundaries, as observed in graphene on Ir(111) (10) and on hBN (13). We investigate this possibility by analyzing energy distribution curve (EDC) cuts at the local band maxima and at the mBZ border, as shown in Fig. 5 (A and B) for the Γ - Γ_m direction. The EDC extracted at the crossing between the main band and a neighboring miniband at the mBZ border exhibits a peak (see blue curve) with no sign of intensity loss in this energy range where a gap would be expected. A similar analysis is carried out for two

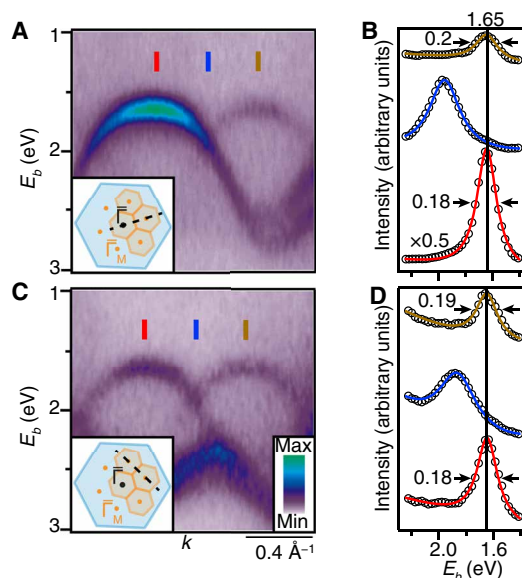


Fig. 5. Analysis of miniband dispersion in θ_1 -domain. (A) Dispersion of the main band and the neighboring miniband obtained along the dashed line shown in the BZ and mBZ sketches in the inset. (B) EDC cuts (markers) extracted at Γ the mBZ border and Γ_m as illustrated by the red, blue, and brown sticks in (A). Correspondingly colored curves represent fits to a Lorentzian peak on a parabolic background. The data extracted at Γ have been scaled by a factor of 0.5. The local maximum of the bands has been marked by a vertical line, and the FWHM is indicated by arrows. Values are given in electron volts and the error bars are ± 0.02 eV. (C) Dispersion of minibands in neighboring mBZs (see dashed line in inset). (D) EDCs (markers) with fits (curves) presented in an identical way as in (B).

crossing minibands in Fig. 5 (C and D), leading to the same conclusion. Moreover, we find that the main band and all minibands exhibit a local maximum at a binding energy of 1.65 eV and a Lorentzian peak shape with a full width at half maximum (FWHM) of (0.18 ± 0.02) eV (see red and brown curves in Fig. 5, B and D), indicating identical quasiparticle dynamics in all the bands. We note that the absence of mini gaps does not rule out the possibility of an initial state effect. The weak interaction between the WS_2 and graphene, which is evident from the lack of hybridization between the main bands of the two materials in Fig. 3C, likely leads to a gapping effect that is too weak to be resolved in our data. Both final and initial state effects may coexist, and if the former is stronger than the latter, then it could also mask the loss of intensity expected to accompany the opening of a gap.

CONCLUSION

In summary, we have directly measured the quasiparticle band structure for a graphene/ WS_2 heterobilayer on hBN using a new x-ray capillary technology for carrying out microARPES. In particular, we capitalize on the 1- μm spatially resolving capabilities afforded by this technique not only to determine different interlayer twist angles between the graphene and WS_2 but also to directly measure minibands and multiple mBZs with periodicities that match the moiré reciprocal lattice vector of our heterobilayer. The technique itself allows for a systematic search of quasiparticle band structures that emerge from moiré superlattices in van der Waals heterostructures. We believe that this is a key observation that not only compliments recent optical studies that have revealed moiré excitons in TMD/TMD

heterobilayers (19–22) but also demonstrates that our microARPES approach is an ideal strategy toward superlattice engineering of band structure and correlations in 2D materials. Tuning the interlayer interaction further via twist angle or choice of 2D material may lead to resolvable mini gaps, which will establish a clear distinction between initial and final state effects in photoemission from heterobilayers. We therefore expect that our results will inspire further experimental and theoretical studies of the interplay of these effects in multifunctional heterobilayer materials.

MATERIALS AND METHODS

Graphene growth on copper foils

Graphene films were grown using low-pressure CVD with flowing H_2 and CH_4 gases (32). Before growth, the copper foils were electrochemically polished to improve surface cleanliness and remove oxides. These copper foils were then folded into “packets” (33), loaded into a quartz tube, and pumped to a base pressure of 2 mtorr. The copper substrates were heated to 1030°C, and H_2/CH_4 was introduced for 1.5 hours at a total pressure of ≈ 60 mtorr. The substrates were then quenched by removing them from the hot zone while under vacuum.

SL WS_2 growth on SiO_2/Si

Synthesis of SL WS_2 was performed at ambient pressure in a 5-cm-diameter quartz tube furnace on SiO_2/Si substrates (275-nm thickness of SiO_2). Before use, all SiO_2/Si substrates were cleaned in acetone, isopropanol, and Piranha etch and then thoroughly rinsed in deionized water. At the center of the furnace, a quartz boat containing 1 g of WO_3 powder was positioned. Two SiO_2/Si wafers were positioned facedown, directly above the oxide precursor. The upstream wafer contained perylene-3,4,9,10-tetracarboxylic acid tetrapotassium salt (PTAS) seeding molecules, while the downstream substrate was untreated. The hexagonal PTAS molecules were carried downstream to the untreated substrate and promoted lateral growth of the TMD materials. A separate quartz boat containing sulfur powder was placed upstream, outside the furnace-heating zone. Pure argon (65 sccm) was used as the furnace was heated to the target temperature. Upon reaching the target temperature of 825°C, 10-sccm H_2 was added to the Ar flow and maintained throughout the 10-min soak and subsequent cooling.

Heterostructure fabrication

Bulk hBN crystals were exfoliated onto a n-doped TiO_2 substrate using Scotch tape to obtain 10- to 30-nm-thick flakes. The TiO_2 substrate with exfoliated hBN flakes was annealed in ultrahigh vacuum (UHV) at 150°C for 15 min to get rid of any unwanted tape residues. Next, CVD-grown single-domain SL WS_2 was transferred onto the cleaned hBN flakes using a thin polycarbonate film on a polydimethylsiloxane stamp using a custom-built transfer tool (26, 34). This was followed by another annealing cycle of the WS_2/hBN heterostructure in UHV at 150°C for 15 min. Separately, one side of the copper foil (with graphene grown on both sides) was spin-coated with a poly(methyl methacrylate) (PMMA) layer. The CVD graphene layer on the backside (without protective PMMA layer) of the copper foil was etched away using reactive ion etching. Next, the PMMA/graphene was floated by etching away the copper using wet chemistry (35, 36). The PMMA/graphene layer was subsequently transferred onto a clean WS_2/hBN stack. The top PMMA layer was removed by immersing the graphene/ WS_2/hBN heterostructure in acetone for

15 min, followed rinsing in isopropanol. Last, the graphene/ WS_2/hBN heterostructure was subjected to another annealing cycle in UHV.

Spatially resolved ARPES experiments

The heterobilayer sample was shipped in air and inserted into the Microscopic and Electronic Structure Observatory (MAESTRO) UHV facility at the Advanced Light Source in Berkeley. The sample was annealed at 600 K for 15 min before ARPES measurements.

The microfocused scanning of the core level and ARPES spectra presented in Figs. 1 and 2 was carried out in the MAESTRO nanoARPES end-station using an x-ray capillary (Sigray Inc.) with a spatial resolution in this experiment given by $\Delta s = (1.83 \pm 0.03) \mu m$, as explained in section S5. We used a coarse-motion piezo scanner for spatial maps larger than 30 μm with a step size of 1.5 μm and a fine-motion piezo flexure scanning stage for detailed maps below this range and with a scanning step of 250 nm. Because of the achromaticity of the capillary, we were able to perform VB measurements with variable photon energy in the range of 60 to 160 eV and W 4f, S 2p, B 1s, and C 1s core level measurements with a photon energy of 350 eV without apparent loss of spatial resolution. The high efficiency of the capillary enabled acquisition of 4D datasets of the (E, k_x, k_y) -dependent intensity in ≈ 40 min. The (E, k_x, k_y) -dependent data presented in Fig. 3 were collected using an electron analyzer equipped with custom-made deflectors in the MAESTRO microARPES end-station, such that the sample could be held fixed during BZ mapping. These measurements were acquired with a photon beam focused to a spot size of $\approx 10 \mu m$ using Kirkpatrick-Baez optics, enabling BZ mapping on a time scale of ≈ 10 min for our flakes. Section S1 demonstrates that high-quality spectra could be collected from θ_1 - and θ_2 -domains using the larger beam on the relevant areas identified by the high-spatial resolution maps in Figs. 1 and 2. All data were obtained using hemispherical Scienta R4000 electron analyzers with the energy and momentum resolution set at 40 meV and 0.01 \AA^{-1} , respectively. The sample was held at room temperature during all the measurements.

SUPPLEMENTARY MATERIALS

Supplementary material for this article is available at <http://advances.sciencemag.org/cgi/content/full/6/14/eaay6104/DC1>

REFERENCES AND NOTES

- M.-H. Chiu, C. Zhang, H.-W. Shiu, C.-P. Chuu, C.-H. Chen, C.-Y. S. Chang, C.-H. Chen, M.-Y. Chou, C.-K. Shih, L.-J. Li, Determination of band alignment in the single-layer $MoSe_2/WSe_2$ heterojunction. *Nat. Commun.* **6**, 7666 (2015).
- N. R. Wilson, P. V. Nguyen, K. Seyler, P. Rivera, A. J. Marsden, Z. P. L. Laker, G. C. Constantinescu, V. Kandyba, A. Barinov, N. D. M. Hine, X. Xu, D. H. Cobden, Determination of band offsets, hybridization, and exciton binding in 2D semiconductor heterostructures. *Sci. Adv.* **3**, e1601832 (2017).
- X. Hong, J. Kim, S.-F. Shi, Y. Zhang, C. Jin, Y. Sun, S. Tongay, J. Wu, Y. Zhang, F. Wang, Ultrafast charge transfer in atomically thin MoS_2/WSe_2 heterostructures. *Nat. Nanotechnol.* **9**, 682–686 (2014).
- C. Zhang, C.-P. Chuu, X. Ren, M.-Y. Li, L.-J. Li, C. Jin, M.-Y. Chou, C.-K. Shih, Interlayer couplings, moiré patterns, and 2D electronic superlattices in MoS_2/WSe_2 hetero-bilayers. *Sci. Adv.* **3**, e1601459 (2017).
- C. R. Dean, L. Wang, P. Maher, C. Forsythe, F. Ghahari, Y. Gao, J. Katoch, M. Ishigami, P. Moon, M. Koshino, T. Taniguchi, K. Watanabe, K. L. Shepard, J. Hone, P. Kim, Hofstadter's butterfly and the fractal quantum Hall effect in moiré superlattices. *Nature* **497**, 598–602 (2013).
- L. A. Ponomarenko, R. V. Gorbachev, G. L. Yu, D. C. Elias, R. Jalil, A. A. Patel, A. Mishchenko, A. S. Mayorov, C. R. Woods, J. R. Wallbank, M. Mucha-Kruczynski, B. A. Piot, M. Potemski, I. V. Grigorieva, K. S. Novoselov, F. Guinea, V. I. Fal'ko, A. K. Geim, Cloning of Dirac fermions in graphene superlattices. *Nature* **497**, 594–597 (2013).
- B. Hunt, J. D. Sanchez-Yamagishi, A. F. Young, M. Yankowitz, B. J. LeRoy, K. Watanabe, T. Taniguchi, P. Moon, M. Koshino, P. Jarillo-Herrero, R. C. Ashoori, Massive Dirac fermions

- and Hofstadter butterfly in a van der Waals heterostructure. *Science* **340**, 1427–1430 (2013).
8. Y. Cao, V. Fatemi, S. Fang, K. Watanabe, T. Taniguchi, E. Kaxiras, P. Jarillo-Herrero, Unconventional superconductivity in magic-angle graphene superlattices. *Nature* **556**, 43–50 (2018).
 9. M. Yankowitz, S. Chen, H. Polshyn, Y. Zhang, K. Watanabe, T. Taniguchi, D. Graf, A. F. Young, C. R. Dean, Tuning superconductivity in twisted bilayer graphene. *Science* **363**, 1059–1064 (2019).
 10. I. Pletikosić, M. Kralj, P. Pervan, R. Brako, J. Coraux, A. T. N'Diaye, C. Busse, T. Michely, Dirac cones and minigaps for graphene on Ir(111). *Phys. Rev. Lett.* **102**, 056808 (2009).
 11. E. Starodub, A. Bostwick, L. Moreschini, S. Nie, F. E. Gabaly, K. F. McCarty, E. Rotenberg, In-plane orientation effects on the electronic structure, stability, and Raman scattering of monolayer graphene on Ir(111). *Physical Review B* **83**, 125428 (2011).
 12. T. Ohta, J. T. Robinson, P. J. Feibelman, A. Bostwick, E. Rotenberg, T. E. Beechem, Evidence for interlayer coupling and moiré periodic potentials in twisted bilayer graphene. *Phys. Rev. Lett.* **109**, 186807 (2012).
 13. E. Wang, X. Lu, S. Ding, W. Yao, M. Yan, G. Wan, K. Deng, S. Wang, G. Chen, L. Ma, J. Jung, A. V. Fedorov, Y. Zhang, G. Zhang, S. Zhou, Gaps induced by inversion symmetry breaking and second-generation Dirac cones in graphene/hexagonal boron nitride. *Nat. Phys.* **12**, 1111–1115 (2016).
 14. E. Wang, G. Chen, G. Wan, X. Lu, C. Chen, J. Avila, A. V. Fedorov, G. Zhang, M. C. Asensio, Y. Zhang, S. Zhou, Electronic structure of transferred graphene/h-BN van der Waals heterostructures with nonzero stacking angles by nano-ARPES. *J. Phys. Condens. Matter* **28**, 444002 (2016).
 15. J. A. Miwa, S. Ulstrup, S. Sørensen, M. Dendzik, A. G. Čabo, M. Bianchi, J. Lauritsen, P. Hofmann, Electronic structure of epitaxial single-layer MoS₂. *Phys. Rev. Lett.* **114**, 046802 (2015).
 16. Y. Zhang, T.-R. Chang, B. Zhou, Y.-T. Cui, H. Yan, Z. Liu, F. Schmitt, J. Lee, R. Moore, Y. Chen, H. Lin, H.-T. Jeng, S.-K. Mo, Z. Hussain, A. Bansil, Z.-X. Shen, Direct observation of the transition from indirect to direct bandgap in atomically thin epitaxial MoSe₂. *Nat. Nanotechnol.* **9**, 111–115 (2013).
 17. M. M. Ugeda, A. J. Bradley, S.-F. Shi, F. H. da Jornada, Y. Zhang, D. Y. Qiu, W. Ruan, S.-K. Mo, Z. Hussain, Z.-X. Shen, F. Wang, S. G. Louie, M. F. Crommie, Giant bandgap renormalization and excitonic effects in a monolayer transition metal dichalcogenide semiconductor. *Nat. Mater.* **13**, 1091–1095 (2014).
 18. C. Kastl, C. T. Chen, R. J. Koch, B. Schuler, T. R. Kuykendall, A. Bostwick, C. Jozwiak, T. Seyller, E. Rotenberg, A. Weber-Bargioni, S. Aloni, A. M. Schwartzberg, Multimodal spectroscopy of monolayer WS₂ enabled by ultra-clean van der Waals epitaxy. *2D Mater.* **5**, 045010 (2018).
 19. E. M. Alexeev, D. A. Ruiz-Tijerina, M. Danovich, M. J. Hamer, D. J. Terry, P. K. Nayak, S. Ahn, S. Pak, J. Lee, J. I. Sohn, M. R. Molas, M. Koperski, K. Watanabe, T. Taniguchi, K. S. Novoselov, R. V. Gorbachev, H. S. Shin, V. I. Fal'ko, A. I. Tartakovskii, Resonantly hybridized excitons in moiré superlattices in van der Waals heterostructures. *Nature* **567**, 81–86 (2019).
 20. C. Jin, E. C. Regan, A. Yan, M. I. B. Utama, D. Wang, S. Zhao, Y. Qin, S. Yang, Z. Zheng, S. Shi, K. Watanabe, T. Taniguchi, S. Tongay, A. Zettl, F. Wang, Observation of moiré excitons in WSe₂/WS₂ heterostructure superlattices. *Nature* **567**, 76–80 (2019).
 21. K. L. Seyler, P. Rivera, H. Yu, N. P. Wilson, E. L. Ray, D. G. Mandrus, J. Yan, W. Yao, X. Xu, Signatures of moiré-trapped valley excitons in MoSe₂/WS₂ heterobilayers. *Nature* **567**, 66–70 (2019).
 22. K. Tran, G. Moody, F. Wu, X. Lu, J. Choi, K. Kim, A. Rai, D. A. Sanchez, J. Quan, A. Singh, J. Embley, A. Zepeda, M. Campbell, T. Autry, T. Taniguchi, K. Watanabe, N. Lu, S. K. Banerjee, K. L. Silverman, S. Kim, E. Tutuc, L. Yang, A. H. MacDonald, X. Li, Evidence for moiré excitons in van der Waals heterostructures. *Nature* **567**, 71–75 (2019).
 23. D. A. Ruiz-Tijerina, V. I. Fal'ko, Interlayer hybridization and moiré superlattice minibands for electrons and excitons in heterobilayers of transition-metal dichalcogenides. *Phys. Rev. B* **99**, 125424 (2019).
 24. J. Kunstmann, F. Mooshammer, P. Nagler, A. Chaves, F. Stein, N. Paradiso, G. Plechinger, C. Strunk, C. Schüller, G. Seifert, D. R. Reichman, T. Korn, Momentum-space indirect interlayer excitons in transition-metal dichalcogenide van der Waals heterostructures. *Nat. Phys.* **14**, 801–805 (2018).
 25. F. Wu, T. Lovorn, E. Tutuc, A. H. MacDonald, Hubbard model physics in transition metal dichalcogenide moiré bands. *Phys. Rev. Lett.* **121**, 026402 (2018).
 26. J. Katoch, S. Ulstrup, R. J. Koch, S. Moser, K. M. McCreary, S. Singh, J. Xu, B. T. Jonker, R. K. Kawakami, A. Bostwick, E. Rotenberg, C. Jozwiak, Giant spin-splitting and gap renormalization driven by trions in single-layer WS₂/h-BN heterostructures. *Nat. Phys.* **14**, 355–359 (2018).
 27. A. Sakdinawat, D. Attwood, Nanoscale x-ray imaging. *Nat. Photonics* **4**, 840–848 (2010).
 28. R. J. Koch, C. Jozwiak, A. Bostwick, B. Stripe, M. Cordier, Z. Hussain, W. Yun, E. Rotenberg, Nano focusing of soft x-rays by a new capillary mirror optic. *Synchrotron Radiat. News* **31**, 50–52 (2018).
 29. C. Kastl, R. J. Koch, C. T. Chen, J. Eichhorn, S. Ulstrup, A. Bostwick, C. Jozwiak, T. R. Kuykendall, N. J. Borys, F. M. Toma, S. Aloni, A. Weber-Bargioni, E. Rotenberg, A. M. Schwartzberg, Effects of defects on band structure and excitons in WS₂ revealed by nanoscale photoemission spectroscopy. *ACS Nano* **13**, 1284–1291 (2019).
 30. B. Amorim, General theoretical description of angle-resolved photoemission spectroscopy of van der Waals structures. *Phys. Rev. B* **97**, 165414 (2018).
 31. C. M. Polley, L. I. Johansson, H. Fedderwitz, T. Balasubramanian, M. Leandersson, J. Adell, R. Yakimova, C. Jacobi, Origin of the π -band replicas in the electronic structure of graphene grown on 4H-SiC(0001). *Phys. Rev. B* **99**, 115404 (2019).
 32. Y. Zhu, S. Murali, M. D. Stoller, K. J. Ganesh, W. Cai, P. J. Ferreira, A. Pirkle, R. M. Wallace, K. A. Cychoz, M. Thammes, D. Su, E. A. Stach, R. S. Ruoff, Carbon-based supercapacitors produced by activation of graphene. *Science* **332**, 1537–1541 (2011).
 33. X. Li, C. W. Magnuson, A. Venugopal, R. M. Tromp, J. B. Hannon, E. M. Vogel, L. Colombo, R. S. Ruoff, Large-area graphene single crystals grown by low-pressure chemical vapor deposition of methane on copper. *J. Am. Chem. Soc.* **133**, 2816–2819 (2011).
 34. S. Ulstrup, J. Katoch, R. J. Koch, D. Schwarz, S. Singh, K. M. McCreary, H. K. Yoo, J. Xu, B. T. Jonker, R. K. Kawakami, A. Bostwick, E. Rotenberg, C. Jozwiak, Spatially resolved electronic properties of single-layer WS₂ on transition metal oxides. *ACS Nano* **10**, 10058–10067 (2016).
 35. A. K. Patra, S. Singh, B. Barin, Y. Lee, J.-H. Ahn, E. del Barco, E. R. Mucciolo, B. Özyilmaz, Dynamic spin injection into chemical vapor deposited graphene. *Appl. Phys. Lett.* **101**, 162407 (2012).
 36. S. Singh, A. Ahmadi, C. T. Cherian, E. R. Mucciolo, E. del Barco, B. Özyilmaz, Dynamical spin injection at a quasi-one-dimensional ferromagnet-graphene interface. *Appl. Phys. Lett.* **106**, 032411 (2015).

Acknowledgments

Funding: S.U. and J.A.M. acknowledge financial support from VILLUM FONDEN (grant no. 15375), from the Danish Council for Independent Research, Natural Sciences under the Sapere Aude program (grant no. DFF-6108-00409), and from Aarhus University Research Foundation. R.J.K. is supported by a fellowship within the Postdoc-Program of the German Academic Exchange Service (DAAD). S.S. and J.K. acknowledge the startup funds from Carnegie Mellon University. J.K. also acknowledges partial support from the Center for Emergent Materials: an NSF MRSEC under award number DMR-1420451. The Advanced Light Source is supported by the Director, Office of Science, Office of Basic Energy Sciences, of the U.S. Department of Energy under Contract No. DE-AC02-05CH11231. The work at NRL was supported by core programs and the Nanoscience Institute. **Author contributions:** S.U., J.K., and J.A.M. designed and planned the project. K.M.M. and B.T.J. synthesized the SL WS₂. J.T.R. prepared CVD graphene on copper, and S.S. and J.K. fabricated the heterostructures. S.U., R.J.K., C.J., E.R., A.B., J.K., and J.A.M. performed the ARPES experiments. R.J.K., C.J., E.R., and A.B. installed and commissioned the x-ray capillary. R.J.K. developed the methodology that formed the basis for analyzing and interpreting the data. S.U. and J.A.M. analyzed the data. All authors contributed to the preparation of the manuscript. **Competing interests:** The authors declare that they have no competing interests. **Data and materials availability:** All data needed to evaluate the conclusions in the paper are present in the paper and/or the Supplementary Materials. Additional data related to this paper may be requested from the corresponding authors.

Submitted 3 July 2019

Accepted 7 January 2020

Published 3 April 2020

10.1126/sciadv.aay6104

Citation: S. Ulstrup, R. J. Koch, S. Singh, K. M. McCreary, B. T. Jonker, J. T. Robinson, C. Jozwiak, E. Rotenberg, A. Bostwick, J. Katoch, J. A. Miwa, Direct observation of minibands in a twisted graphene/WS₂ bilayer. *Sci. Adv.* **6**, eaay6104 (2020).